Thermal Science and Engineering Progress 51 (2024) 102635

Contents lists available at ScienceDirect

Thermal Science and Engineering Progress

journal homepage: www.sciencedirect.com/journal/thermal-science-and-engineering-progress

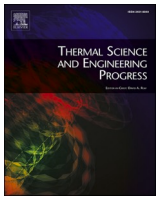

Durable and reliable thermal management system with superior temperature uniformity for sidewall coring tool in extreme thermal environments

Jiale Peng [a], Zhibin Tian [b], Chao Deng [a], Fulong Wei [a], Bofeng Shang [c,*], Xiaobing Luo [a,*]

[a] School of Energy and Power Engineering, Huazhong University of Science and Technology, Wuhan, China
[b] Well-Tech Research Institute of China Oilfield Service Limited, Beijing, China
[c] School of Physics and Microelectronics, Zhengzhou University, Zhengzhou, China

ARTICLE INFO

Keywords:
Sidewall coring tool
Thermal management system
Extreme thermal environments
Operational duration
Heat storage module
Reliability

ABSTRACT

The sidewall coring tool (SCT) plays a crucial role in exploring the distribution of oil and gas resources, which needs to operate in a challenging high temperature (205 °C) and vibrating downhole environment for 21 h. However, the internal electronics are unable to withstand such extreme temperatures. Previous investigations on thermal management of downhole electronics have failed to ensure long operational duration and reliability. To solve this issue, a durable and reliable thermal management system (TMS) with superior temperature uniformity was proposed for the SCT in this paper. First, the proposed system adopted heat storage modules (HSMs) with high heat storage density and heat diffusion coefficient to enhance the heat storage rate and extend the operational duration. Second, HSMs were utilized for storing heat from nearby heat sources to improve temperature uniformity. Meanwhile, the reliability of HSMs was verified by high-temperature vibration experimental tests. Finally, through iterative optimization, the system utilized a well-designed configuration of thermal insulators and HSMs to further improve temperature uniformity, thereby extending the operational duration of the system. The performance of the total system was evaluated by thermal simulations. The maximum temperature of the heat sources remained below 150 °C after 21 h, with a maximum temperature difference between any two sources not exceeding 12 °C. Furthermore, the experiment was conducted to validate the simulated results, with the relative error within 5 %. The proposed TMS demonstrates a significantly extended operational duration and improved reliability compared to previous works, which has been successfully applied to downhole operations.

1. Introduction

With the increasing global demand for petroleum resources and the depletion of shallow oil and gas reserves, the exploration of deeper and hotter wells has become increasingly appealing [1–4]. Indeed, geological research indicates that downhole temperatures increase by approximately 1 to 9 °C per 100 m [5–7]. This information suggests that downhole temperatures could potentially exceed 200 °C in certain conditions. The SCT is utilized in downhole coring operations to acquire core samples [8,9], enabling the assessment of oil and gas resources within the well [10,11]. The SCT is highly valuable in the field of petroleum exploration due to its direct access capability to retrieve the cores from the bottom of the well. Fig. 1 illustrates the structure of SCT, which comprises four main cartridges: the electronic cartridge, tension cartridge, bridle cartridge, and mechanical hydraulic cartridge. In the operational process, the electronic cartridge controls the mechanical hydraulic cartridge for executing coring action. The high-speed drills used for coring in the mechanical-hydraulic cartridge are driven by hydraulic system motors, which are controlled by devices in the electronic section. For this tool, the maximum number of cores acquired per operation is 60, whereas at least 3 cores are obtained in 1 h. In addition, the time spent on lowering and lifting the tool is about 1 h. Therefore, the SCT is expected to operate continuously for 21 h at a downhole temperature of 205 °C while enduring vibrations [12]. Among these cartridges, the electronic cartridge is particularly sensitive to temperature due to its high concentration of electronics. Under the dual impact of the high-temperature environment and the heat generated by the electronics, the electronics are susceptible to failure, potentially leading to significant accidents. High-temperature electronics cannot be widely

* Corresponding authors.
E-mail addresses: shangbofeng@zzu.edu.cn (B. Shang), Luoxb@hust.edu.cn (X. Luo).

https://doi.org/10.1016/j.tsep.2024.102635
Received 3 February 2024; Received in revised form 5 May 2024; Accepted 11 May 2024
Available online 12 May 2024

Nomenclature

ρ	Density
c	Specific heat capacity
λ	Thermal conductivity
T	Temperature
t	Time (min)
q	Power per unit volume
k	Thermal conductivity
c_{eff}	Equivalent heat capacity of PCM
V	Volume
α	Volume fraction of liquid PCM
h_L	Average convective heat transfer coefficient
r_h	Radius of the wellbore wall
r_t	Radius of the logging tool
L	Length of the logging tool
a	Thermal diffusion coefficient
$u(T)$	Uncertainty in temperature measurement
m	Uncertainty in thermocouple temperature measurement
n	Uncertainty in temperature measurement by data acquisition instrument
$Q_{storage}$	The heat storage
$Q_{storage\text{-}HSMs}$	The heat storage of HSMs
$Q_{storage\text{-}others}$	The heat storage of other parts
Q_{heat}	The heat generated by heat sources
$Q_{environemnt}$	The heat leakage from environments
H	Enthalpy
H_0	Initial enthalpy

Subscripts

PCM-s	Solid PCM
PCM-l	Liquid PCM
s	Start of phase change
l	End of phase change

Abbreviations

SCT	Sidewall coring tool
TMS	Thermal management system
HSM	Heat storage module
PCM	Phase change material
PTMS	Passive thermal management system
PEEK	Polyetheretherketone
CFD	Computational fluid dynamics

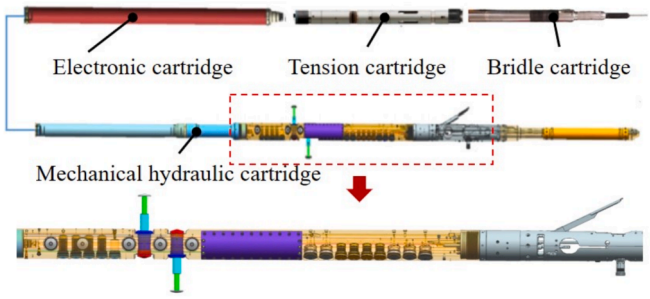

Fig. 1. The structure of SCT.

applied on the SCT because of their high cost [13,14]. Consequently, an effective TMS is essential to safeguard the SCT, ensuring durable and reliable operation under challenging temperature conditions [15,16].

Many scholars have proposed TMS for downhole electronics, including active and passive cooling technologies. Extensive researches have been conducted on various active cooling methods such as vapor compression refrigeration, thermoelectric refrigeration, thermoacoustic refrigeration, liquid cooling, split-Stirling refrigeration. Wei et al. [17] developed an active cooling system that effectively reduced the temperature of electronics to below 165 °C in a 200 °C environment. Building upon Wei's work, Tao et al. [18] further achieved a temperature reduction to 154.1 °C through vapor compression refrigeration. Soprani et al. [19] optimized a downhole thermoelectric cooling system, successfully maintaining the temperature of 1 W electronics below 170 °C for continuous 200 h at 200 °C. Weerasinghe et al. [20] designed a high-temperature downhole thermoelectric cooling system, successfully cooling downhole electronic devices to around 130 °C at an ambient temperature of 160 °C. Tang et al. [21] conducted a study on thermoacoustic refrigeration, exploring the impact of various parameters on its performance. Ma et al. [22] introduced an active cooling system incorporating liquid cooling and phase change materials (PCM), extending the operating time to 5 h. Peng et al. [23] proposed a hybrid thermal system integrating liquid cooling and PCM, which significantly reduced the temperature difference between the electronics and PCM. Additionally, Tang et al. [24] and Gao et al. [25] conducted theoretical investigations on the influence of split-Stirling refrigeration. However, these systems face challenges in high-temperature vibration environments due to their energy input requirements and moving parts, making their reliability uncertain for large-scale applications.

As an alternative, PTMSs for logging tools have gained more attention due to their high reliability and integration, which are composed of vacuum flasks [26,27], insulators [28,29], PCMs [30,31], electronics, and skeletons. Among them, a vacuum flask combined with insulators are utilized to minimize heat transfer from high-temperature environments. PCMs between the skeleton and insulators absorb heat generated by electronics, allowing the logging tool to operate safely for extended periods in high-temperature wells. Ma et al. [32] proposed a PTMS combining PCM and a vacuum flask, maintaining electronics below 120 °C for 6 h at an ambient temperature of 200 °C. Building upon this work, Shang et al. [33] further reduced the temperature of electronics by enhancing heat transfer between the electronics and PCM using heat pipes. Peng et al. [34] established a heat transfer channel between electronics and PCM, enabling the electronics to remain below 120 °C for 9 h at an ambient temperature of 205 °C. Lan et al. [35] introduced a distributed heat storage system for a multi-heat source logging tool to extended instrument working time. However, the maximum temperature difference between two heat sources exceeded 40 °C, which limited further operation of the instrument. Zhang et al. [36] optimized the heat insulation and storage of the logging tool, reducing electronics temperature from 163.1 °C to 123 °C after 6 h of operation at 200 °C. He et al. [37] proposed a hybrid TMS with PCM and insulation materials, extending the operating time to approximately 50 min under an ambient environment of 150 °C. Although these TMSs demonstrate potential under specific conditions, their operational duration for sustained downhole operations is limited, particularly for the SCT. The maximum temperature difference between heat sources is too large for logging tools with multiple heat sources. Consequently, it has become imperative to design a durable TMS with superior temperature uniformity for SCT. In addition, the leakage of PCMs may paralyze system electronics and cause serious accidents. Given the high-temperature and vibration environment during SCT operations, dependable HSMs with high-temperature vibration reliability are essential to store the heat generated from electronics.

To ensure reliability in high-temperature vibration environments, a

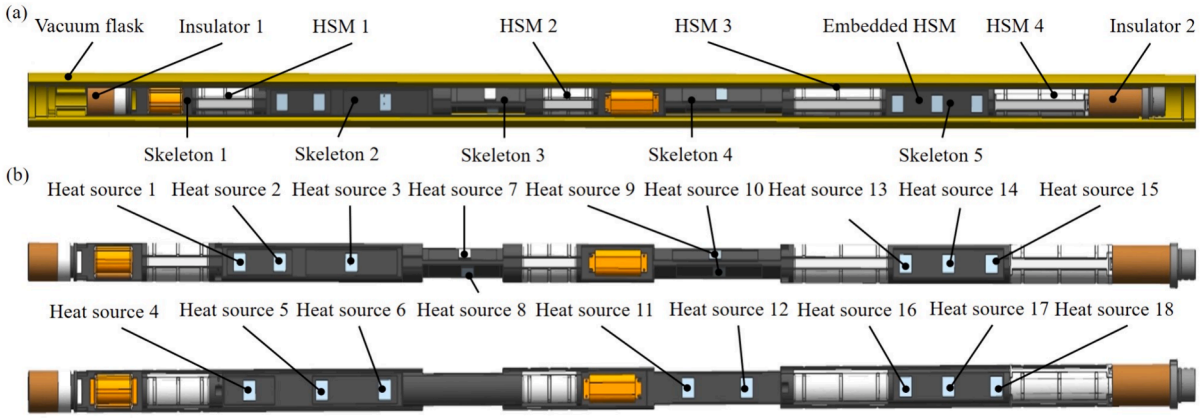

Fig. 2. The structure of the electronic cartridge with TMS. (a) Overall layout; (b) Distribution of heat sources.

Table 1
Heating power distribution of the heat sources.

Component	Heating power (W)	Component	Heating power (W)	Component	Heating power (W)
Heat source 1	1	Heat source 7	3	Heat source 13	3
Heat source 2	2	Heat source 8	2	Heat source 14	4
Heat source 3	1.5	Heat source 9	3	Heat source 15	3
Heat source 4	5	Heat source 10	4	Heat source 16	3
Heat source 5	1.5	Heat source 11	2	Heat source 17	4
Heat source 6	2	Heat source 12	2	Heat source 18	3
Total power					49

Table 2
Materials and thermal properties of the TMS for the SCT [31].

Name	Material	Thermal conductivity ($W \cdot m^{-1} \cdot K^{-1}$)	Density ($kg \bullet m^{-3}$)	Heat capacity ($J \bullet kg^{-1} \bullet K^{-1}$)
Vacuum flask	TC11	7.5	4480	550
Vacuum layer	Composite	0.0002	100	1200
Skeleton	Aluminum alloy	130	2810	960
Heat sources	Ceramic	20	2145	750
Insulator shell	PEEK	0.25	2200	1000
Insulator core	Nano-aerogel	0.025	250	502.3

durable and reliable TMS with superior temperature uniformity for SCT was proposed in this study. High thermal conductivity and high heat storage PCMs, primarily Wood alloys, were utilized to absorb the heat generated by electronics, which extended the operational duration. Additionally, distributed HSMs were utilized to store heat from nearby heat sources to improve temperature uniformity, and the reliability of HSMs was verified by experimental tests. Finally, a rational arrangement of insulators and HSMs was employed through iterative optimization to further enhance temperature uniformity, thereby extending the system's operational duration. High and low-temperature cycling test as well as high-temperature vibration tests were carried out to verify the reliability of the HSMs. Finally, the thermal performance of the proposed thermal management system was validated through simulations and experiments.

2. System composition

2.1. Thermal management system

Due to the temperature sensitive of the electronic cartridge in the SCT, thermal management measures were implemented for its protection. Fig. 2 shows the structure of the electronic cartridge with TMS. The vacuum flask was utilized to insulate against high-temperature and high-pressure downhole environment. The outer and inner diameters of the vacuum flask were 120 mm and 85 mm, respectively, with the length of 4092.5 mm. The vacuum flask was made of TC-11 with a 3-mm thick vacuum layer, which provided excellent pressure-bearing capacity and thermal insulation. However, the heat from high-temperature environment still intruded into the vacuum flask through the two opening ends.

To counter heat intrusion, two insulators were placed at both ends of the vacuum flask. The insulator 1 was made of PEEK to prevent the heat transfer from high-temperature environment through the small opening of the vacuum flask. In contrast, the insulator 2 was located in the large opening, which was more susceptible to the influence of the high-temperature environment. Therefore, the insulator 2 was made of a PEEK shell combined with nano-aerogel to further enhance the thermal insulation performance. Between these two insulators, 18 heat sources were mounted within the skeletons, collectively generating 49 W of heat. The specific heating power distribution of the heat sources were listed in Table 1. A key component of the system was the HSM, comprised of a shell and PCM. These HSMs were strategically positioned based on the heat source distribution, ensuring efficient heat storage and improving temperature uniform. For instance, dedicated HSMs (HSM 4 and HSM 5) were placed in areas where a lot of heat was produced such as skeleton 5 which generated 20 W and was located near a large opening on the vacuum flask. Furthermore, an embedded HSM within skeleton 5 further enhanced heat storage in this critical zone. The physical parameters of part structural materials are shown in Table 2.

It is worth noting that the system's design underwent rigorous optimization, resulting in specific dimensions for insulators, HSMs, and other components. This approach guaranteed the stability and reliability of the electronic cartridge within the SCT, ensuring optimal performance and longevity in the challenging downhole environment. Concretely, the Nelder-Mead algorithm [36] was utilized to ensure a consistent overall system length. The Nelder-Mead algorithm was an optimization algorithm for solving local minima of multivariate functions that did not require the function to be derivable and converged to a

Table 3
Critical size of all components.

Name	Length (mm)	Diameter (mm)	Thick (mm)
Vacuum flask	4092.5	120 and 85	/
Vacuum layer	/	/	3
Skeleton 1	270.5	83	/
Skeleton 2	627.5	83	/
Skeleton 3	398.5	83	/
Skeleton 4	703	83	/
Skeleton 5	393	83	/
HSM 1	201	83	/
HSM 2	177	83	/
HSM 3	307	83	/
HSM 4	333.5	83	/
Embedded HSM	364	/	50 × 25
Insulator 1	95.5	83	/
Insulator 2	187	83	/

local minimum relatively quickly. The objective function of the optimization was to minimize the maximum temperature of heat sources. The constrains were that the total length of the insulators and the HSMs remained unchanged, and the lengths of the insulators and HSMs were systematically adjusted through iterations to attain a well-design with the most uniform temperature distribution. After optimization, the final lengths of the insulator 1, HSM 1, HSM 2, HSM 3, HSM 4, and insulator 2 were adjusted to 95.5 mm, 201 mm, 177 mm, 307 mm, 333.5 mm, 187 mm, respectively. The critical final sizes of all components are shown in Table 3.

In summary, distributed HSMs and thermal optimization were utilized in the proposed system to achieve superior temperature uniformity, thus extending the operational duration.

2.2. Selection of PCM

The selection of PCM significantly impacts the temperature control performance of HSM in the TMS. Low temperature melting alloys and paraffins are commonly utilized for heat storage [38–41], with latent heat thermal storage constituting a substantial portion of total heat storage. To evaluate the properties of these PCMs, specific heat capacity, phase transition temperature, latent heat, density, and thermal conductivity were examined by using specialized instruments.

Differential Scanning Calorimeter (DSC2500, TA Instruments), was conducted to detect the specific heat capacity, phase transition temperature, and latent heat of the selected PCMs. Fig. 3 shows the DSC test curves for the selected PCMs. For the wood alloy, the phase change interval was observed to be 71.3 °C-75.8 °C, with a latent heat of 38400 J/kg. The specific heat capacity was 132 J/(kg·K) in its solid state and 138 J/(kg·K) in its liquid state. In contrast, paraffin exhibited a phase change interval between 71.1 °C and 74.0 °C, with a significantly higher latent heat of 251400 J/kg. Remarkably, paraffin displayed a consistent specific heat capacity of 2000 J/(kg·K) in both its liquid and solid states.

Moreover, the heat storage properties of PCMs are also influenced by their density and thermal conductivity. A densitometer (XFMD-1201S, Hunan Lichen Instrument Science and Technology Co., Ltd.) was used to measure the density of the PCMs, and a laser flash thermal conductivity meter (LFA467, NETZSCH) was utilized to test the thermal conductivity of the PCMs. Table 4 shows the thermophysical properties of the PCMs. The density of the solid and liquid wood alloy was measured at 9660 kg/m^3, with a thermal conductivity of 18.42 W/(m·K). In comparison, the solid and liquid densities of paraffin were 880 kg/m^3 and 770 kg/m^3, respectively, with a thermal conductivity of 0.2 W/(m·K). Additionally, the heat diffusion coefficient, a crucial factor in transient heat storage processes, was calculated. The wood alloy exhibited a heat diffusion coefficient of 14.40 mm^2/s, more than ten times higher than that of paraffin, indicating its superior capability for faster heat storage in wood alloy.

Considering the limited space available, it was essential to consider the heat storage density. Wood alloy outperformed paraffin in this aspect, with a heat storage density reaching 371.92 J/cm^3, almost twice that of paraffin. Based on these considerations, the wood alloy was selected for HSM 1, HSM 3, HSM 4, and embedded HSM due to its superior heat storage density and heat diffusion coefficient. The paraffin was chosen for HSM 2 due to its lower heating power in close proximity which aided in weight reduction. These selections were made to optimize the HSMs for efficient temperature control in the specified application.

2.3. Packaging and testing of HSMs

Once the selection of PCMs was finalized, the next steps involved encapsulation and rigorous testing to avoid PCMs leakage. Considering

Table 4
The thermophysical properties of the PCMs.

PCM	Wood alloy	paraffin
Density (kg/m^3)	9660	880(s) 770(l)
Specific heat capacity(J/(kg·K))	132(s) 138(l)	2000
Phase transition interval(°C)	71.3 °C–75.8 °C	71.1 °C–74.0 °C
Latent heat (J/kg)	38,500	251,400
Thermal conductivity(W/(m·K))	18.42	0.2
Thermal diffusion coefficient	14.40	0.13
Latent heat per unit volume (J/cm^3)	371.92	193.58

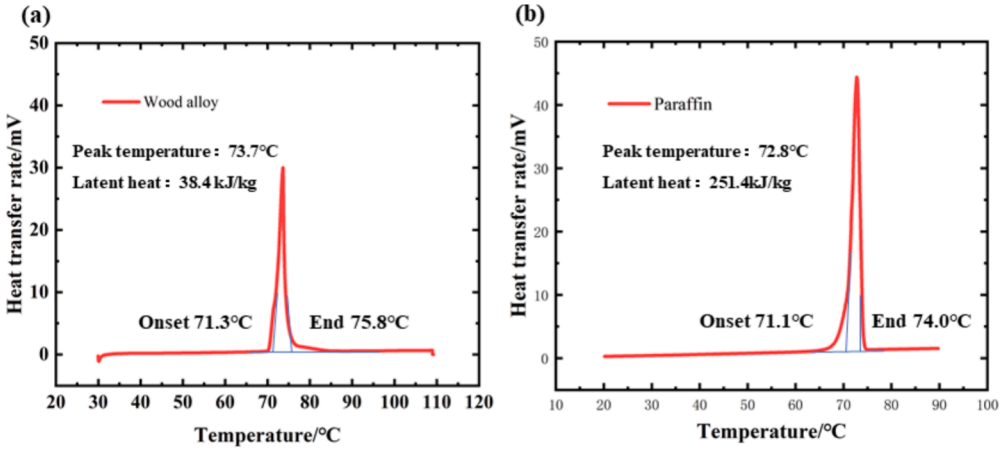

Fig. 3. The DSC test curves for the two PCMs. (a) wood alloy; (b) Paraffin.

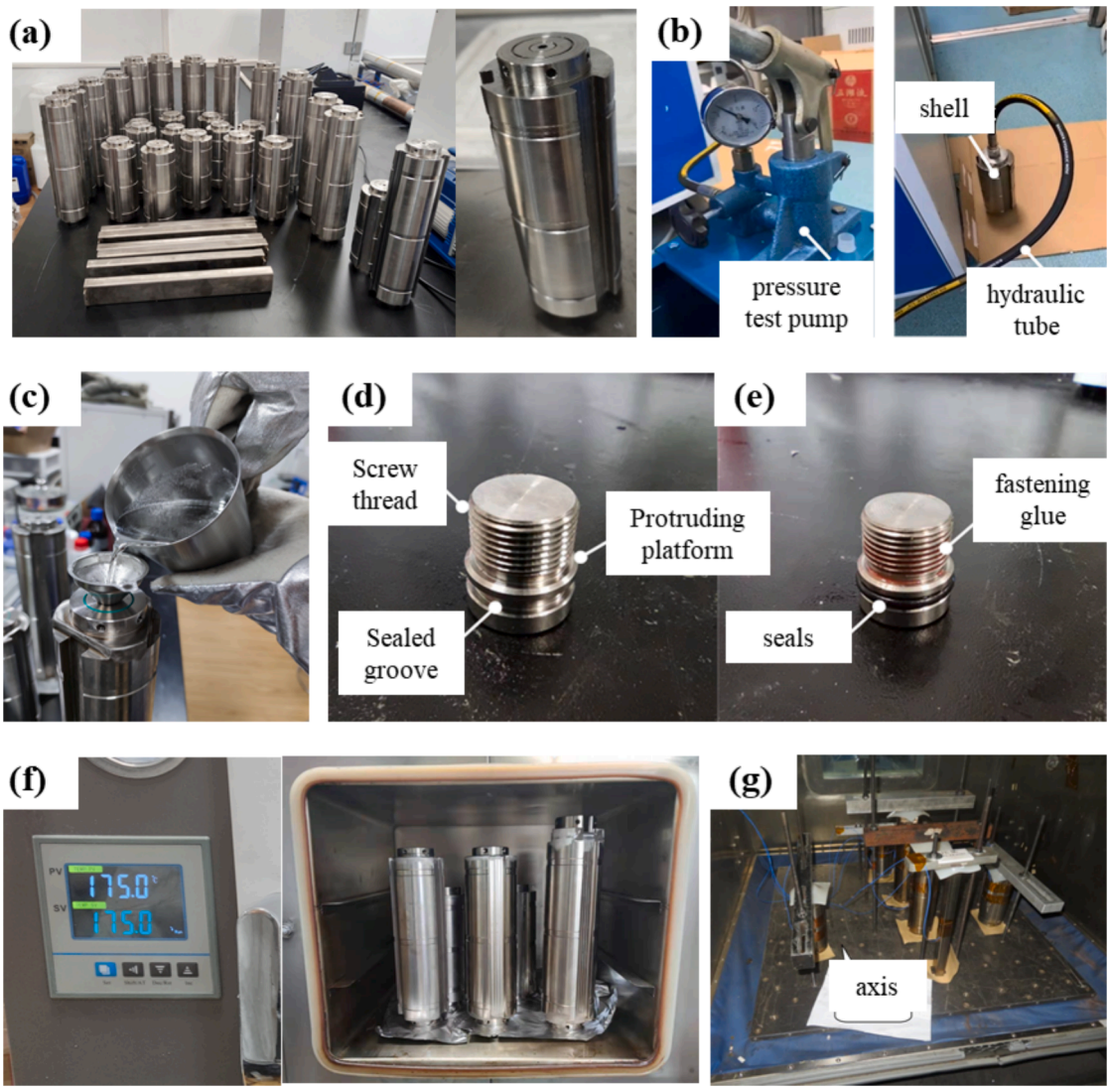

Fig. 4. The packaging and testing for the HSMs. (a) the shell of the HSMs; (b) the pressure resistance test of shell; (c) filling of the PCMs in the HSMs; (d-e) specialized sealing heads; (f) the high and low-temperature cycling test; (g) the high-temperature vibration test.

the challenging downhole conditions involving high temperatures and vibrations, a metal shell was employed for PCM encapsulation. This metal shell, fabricated through welding, featured a hollow interior to encapsulate the PCM, as illustrated in Fig. 4(a). The end of the HSM was pre-sealed with a potting seal. To assess the mechanical strength of the metal shell, a test pump pressurized water to 5 MPa, evaluating the reliability of the weld, as depicted in Fig. 4(b).

Following successful testing of the metal shell, the PCM was melted and encapsulated by a potting seal, as demonstrated in Fig. 4(c). It is important to note that the space within the HSM was allocated for the expansion of PCMs. Specialized sealing heads, depicted in Fig. 4(d) and Fig. 4(e), were employed for sealing, utilizing threads, seals, and sealing protruding platforms.

The HSMs underwent high and low-temperature cycling tests as well as high-temperature vibration tests to assess their reliability and suitability for downhole applications. The tests involved subjecting the HSMs to extreme temperatures and vibrations to evaluate their performance under harsh conditions, detailed in Fig. 4(f) and Fig. 4(g). During the high and low-temperature cycling test, the HSMs were exposed to a temperature of 175 °C for 21 h, followed by cooling to room temperature and then reheating for a total of 50 cycles.

In the high-temperature vibration test, the HSMs were first heated to 150 °C at an oven temperature rise rate of 40 °C/min and maintained for 1 h to ensure that the internal PCM in the HSMs completed the phase change. Subsequently, the vibration platform was turned on to vibrate at an acceleration of 5 g for 15 min, and then increased to 10 g for 15 min. The frequency of vibration test was random vibration frequency to simulate the actual downhole working conditions, and the range was 10–5000 Hz. Axial and radial vibration tests were performed according to the above conditions. The results indicated that the mass of the HSMs remained unchanged before and after testing, and there were no noticeable deformations on their surfaces. These findings demonstrated the reliability of the HSM and confirm its suitability for use in downhole TMSs. This indicates that the encapsulated HSMs can withstand extreme temperature fluctuations and vibrations without undergoing significant changes or damage.

3. Methods

3.1. Simulation setup

To evaluate the performance of the TMS of the SCT, a detailed numerical heat transfer model was developed. The following assumptions were considered to efficiently and accurately simulate the transient heat transfer process:

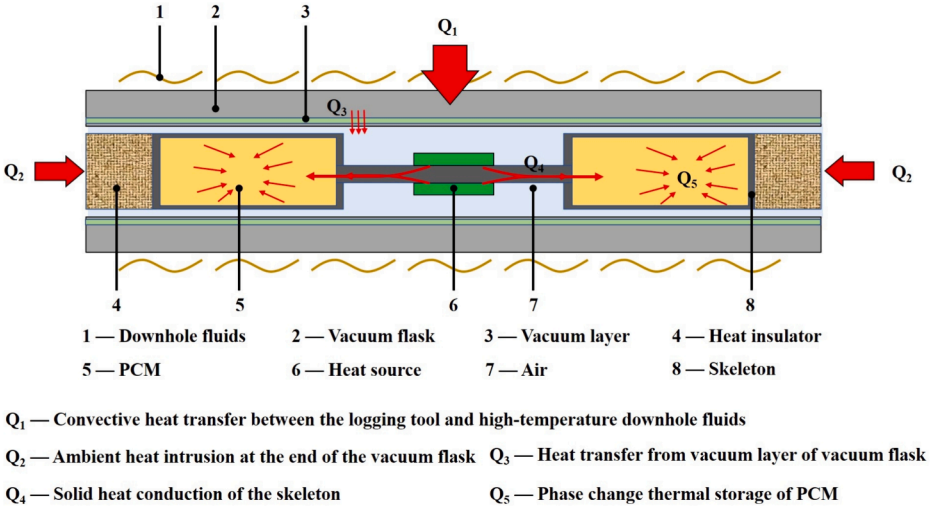

Fig. 5. The simplified schematic diagram of the heat transfer processes of the TMS.

(1) The heat transfer process within the vacuum layer was simplified by treating it as a solid with exceptionally low thermal conductivity [26].
(2) Convective and radiative heat transfer inside the vacuum flask were neglected to simplifiy calculations [31].
(3) Contact thermal resistance was neglected for computational simplicity [35].
(4) Any variations in material properties due to temperature changes were not considered [23,42].
(5) The electronics were considered uniform heat sources, emitting a consistent amount of heat that contributed to the overall thermal dynamics of the system.

Based on the above assumptions, the heat transfer inside the vacuum flask was simplified to a transient heat conduction problem containing internal heat sources. Fig. 5 shows a simplified schematic diagram of the heat transfer processes of the TMS. It contained complex heat transfer processes. The governing equations can be express as follow.

The heat transfer from vacuum layer of vacuum flask was considered to be a solid layer with a thermal conductivity of 0.0002 W/(m·K) [26].

The solid heat conduction of the skeleton, insulators and vacuum flask was expressed as:

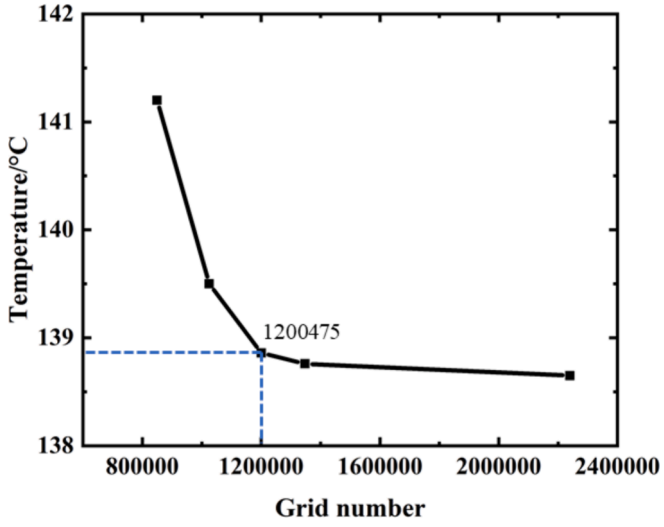

Fig. 6. Grid- independent verification curves.

$$\rho c\frac{\partial T}{\partial t}=\nabla\cdot(k\nabla T)+q \tag{1}$$

Given the nonlinear nature of the phase change process, it was calculated using the equivalent heat capacity method [43]. The equivalent heat capacity of PCMs was expressed as:

$$c_{eff}=\begin{cases} c_{PCM-S} & (T<T_s)\\ \dfrac{1}{\rho}\left[(1-\alpha)\cdot\rho_{PCM-S}\cdot c_{PCM-S}+\alpha\cdot\rho_{PCM-L}\cdot c_{PCM-L}\right]+\dfrac{L_m}{T_l-T_s} & (T_s\leqslant T\leqslant T_l)\\ c_{PCM-L} & (T_l<T)\end{cases} \tag{2}$$

The equivalent density was determined as:

$$\rho_{PCM}=(1-\alpha)\cdot\rho_{PCM-S}+\alpha\cdot\rho_{PCM-L} \tag{3}$$

The equivalent thermal conductivity was represented as:

$$k_{PCM}=(1-\alpha)\cdot k_{PCM-S}+\alpha\cdot k_{PCM-L} \tag{4}$$

α is a function of temperature. It was expressed as:

$$\alpha=\begin{cases} 0 & (T<T_s)\\ \dfrac{V_{PCM-L}}{V_{PCM-L}+V_{PCM-S}} & (T_s\leqslant T\leqslant T_l)\\ 1 & (T_l<T)\end{cases} \tag{5}$$

Additionally, convective heat transfer between the metal vacuum flask and the high-temperature environment was considered. The average convective heat transfer coefficient was expressed as [26]:

$$h_L=\frac{1}{L}\int_0^L h(x)$$
$$=\frac{3k_{\mathrm{mud}}}{4}\left[\frac{\mathrm{U}}{45(r_h-r_t)^2aL}\right]^{\frac{1}{3}}\left[(11r_h-5r_t)^{\frac{1}{3}}+\left(\frac{29r_h-5r_t}{16}\right)^{\frac{1}{3}}\right] \tag{6}$$

In the simulation process, the COMSOL software was employed to solve the numerical 3D model. Initially, the governing equations described in the previous section were incorporated into the CFD solver. Following this, the 3D model for the logging tool was imported into the solver, and an unstructured tetrahedral mesh was generated. Finally, the materials and thermal properties of each component were defined, as detailed in Table 2.

It is noting that the vacuum layer within the metal vacuum flask was treated as a solid layer with a thermal conductivity of 0.0002 W/(m·K)

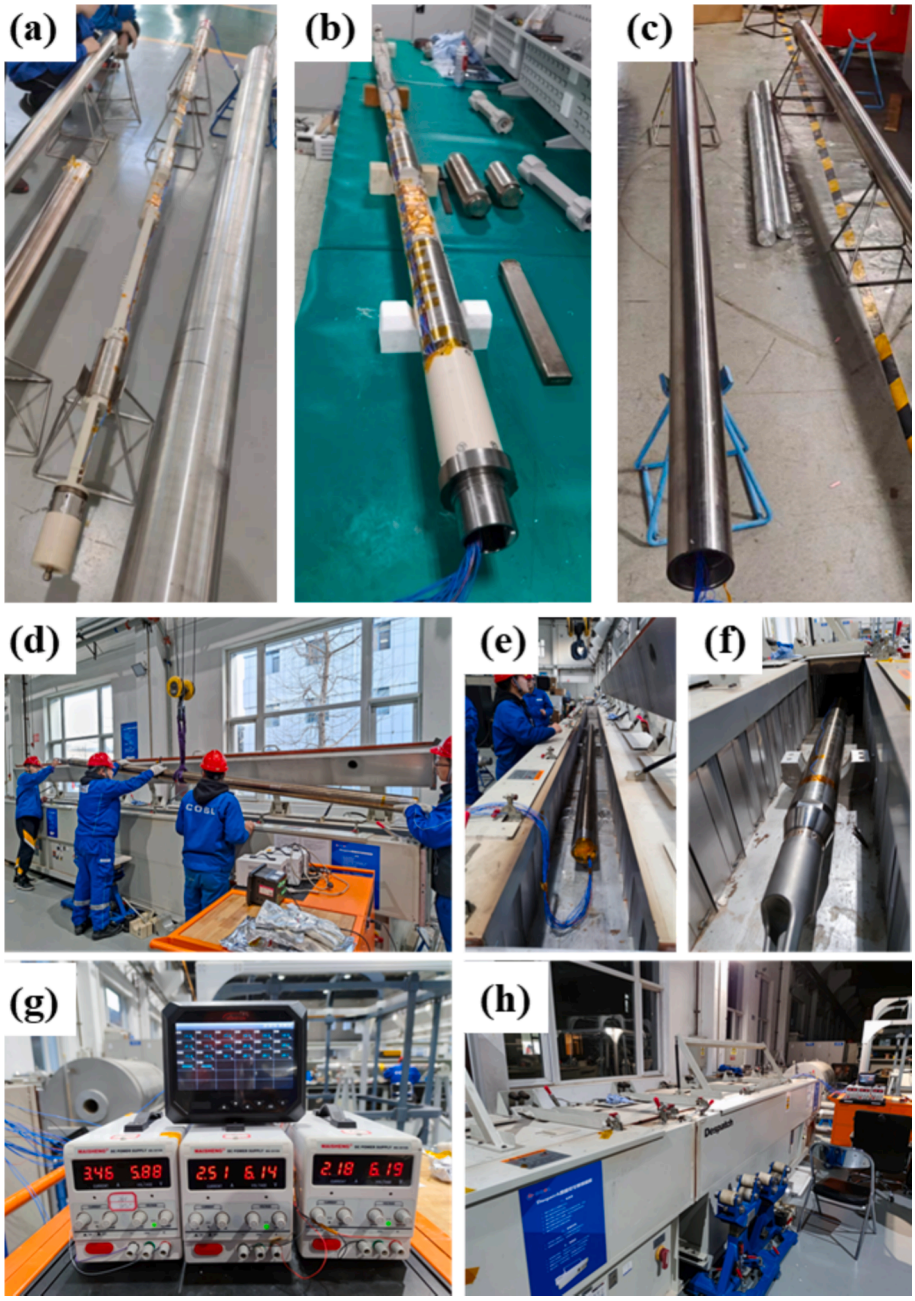

Fig. 7. Experimental test: (a) the actual prototype; (b) the layout of the prototype with heat sources and thermocouples; (c) the vacuum flask loaded with prototype; (d)-(f) the vacuum flask in the ovens; (g) DC power supplies and the data acquisition instrument used for the test; (f) the test site.

[26]. The heating power of heat sources were set according to Table 1. The convective heat transfer boundary condition was applied to the external surface of the vacuum flask, with an ambient temperature set at 205 °C. The initial temperature of the logging tool was established at 20 °C. Utilizing the transient CFD solver, the heat transfer process of the logging tool was calculated from 0 to 1260 min, with a time step of 10 min.

To ensure the accuracy of the calculated results, a grid-independence analysis was conducted. Various numerical models with grid numbers of 849347, 1025369, 1200475, 1347443, and 2,239,851 were evaluated. The maximum temperature of the heat sources in these calculations are presented in Fig. 6. Considering the balance between calculation accuracy and computational resources, the numerical calculation results obtained with a grid number of 1,200,475 were selected for subsequent analysis. The orthotetrahedron meshes were used with a minimum cell size of 16.14 mm. A relative tolerance of 0.0001 and the tolerance factor was 0.1 with the absolute tolerance of 0.00001. The computation converged when the difference between the iterative solutions was less than the absolute tolerance.

3.2. Experimental setup

To validate the simulation, an experimental test was conducted on the TMS for SCT. The prototype including the vacuum flask, skeletons, HSMs, insulators, and others were manufactured according to the one-to-one design, as depicted in Fig. 7(a). For the temperature experiment, two preparations were made. Firstly, ceramic heating elements (40 mm × 40 mm × 2 mm, customizable heat power, Beijing Youpu Science and Technology Centre) were employed as simulated heat sources, which was powered by DC power supplies. These elements were

Table 5
The temperature measurement points in the TMS.

Temperature measurement point	Component	Temperature measurement point	Component	Temperature measurement point	Component
1	Insulator 1	7	Heat source 7	13	HSM 4
2	Skeleton 1	8	Heat source 8	14	Insulator 2
3	HSM 1	9	HSM 2	15	Environment
4	Heat source1	10	Heat source 10	16	Vacuum flask
5	Heat source 3	11	HSM 3		
6	Heat source 5	12	Heat source 14		

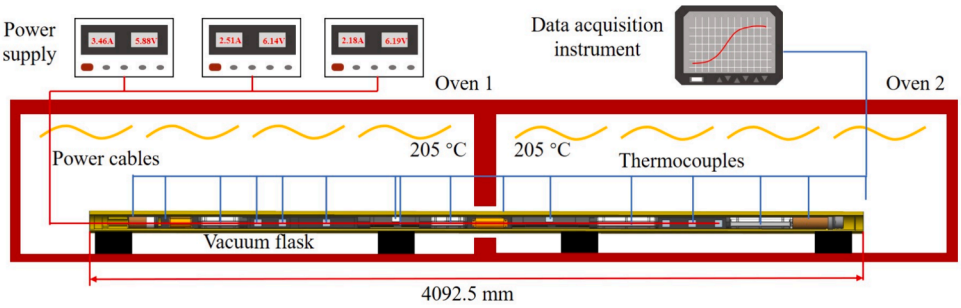

Fig. 8. The schematic diagram illustrating the experimental setup.

affixed to the skeleton using thermal interface materials (2 W·m-1·K-1, XK-P20S20, GLPOLY). Secondly, thermocouples (K-Type, 2 × 0.3 mm, accuracy 0.4 %) were fixed at 16 measuring points, including the outer surface of the vacuum flask, insulators, various simulated heat sources, and the PCM modules, as shown in Table 5. The layout of the prototype with heat sources and thermocouples are shown in Fig. 7(b).

Subsequently, the prototype with simulated heat sources and thermocouples was placed inside a vacuum flask (Xi'an Yufeng Electronic Engineering Company, China), as shown in Fig. 7(c). The prototype and the vacuum flask were then placed inside the ovens (operating range 51 °C-260 °C, PTC1-40, Despatch) as illustrated in Fig. 7(d) – (f). The oven temperature was precisely set to 205 °C, and the experiment was conducted for 21 h. Temperature data was meticulously recorded using a data acquisition instrument (Accuracy 0.2 % ±1 °C, MIK-6000F, Hangzhou Meacon Automation Technology Company) with a sampling period of one second. The DC power supplies and the data acquisition instrument used for the test are depicted in Fig. 7(g), and the test site is shown in Fig. 7(h). Notably, due to the length of the prototype, a combination of two ovens was utilized for the test. Fig. 8 provides a schematic diagram illustrating the experimental setup. These rigorous procedures and measurements were undertaken to ensure the accuracy and reliability of the experimental validation process.

To determine the accuracy of the experimental results, the uncertainty of the temperature measurements was analyzed. The measurement uncertainty for K-Type thermocouples was provided by the producer, which was ± 0.4 %. This means a maximum measurement error of 0.6 °C at a measurement temperature of 150 °C. The total measurement uncertainty was not only due to the tolerance of the thermocouples but also the data acquisition instrument. The measurement uncertainty of the data acquisition instrument was 0.2 % of reading ± 1 °C. The maximum measure error of the data acquisition instrument was 1.3 °C at a measurement temperature of 150 °C. To consider both the thermocouples error and the data acquisition instrument error in the analysis of the results, the following formula was applied:

$$u(T) = \sqrt{m^2 + n^2} \tag{7}$$

Based on Eq. (7), the temperature reading uncertainty obtained in experiments was estimated to be ± 1.43 °C when the measurement temperature was 150 °C.

4. Results and discussion

4.1. Temperature uniformity

Fig. 9 shows the temperature contours of the TMS for SCT at the final moment (21 h). The colours represent the magnitude of the temperature, with red indicating the highest temperature. Elevated temperatures are observed at the ends, while the skeletons and HSMs maintain relatively lower temperatures. Insulator 2 is situated on the side of the large opening of the vacuum flask, where ambient heat transfer is severe, resulting in elevated temperatures. However, owing to its exceptional thermal insulation properties, the high-temperature external environment minimally impacts the internal HSMs and skeletons. Furthermore, the temperatures of the heat sources and skeletons surpass those of the

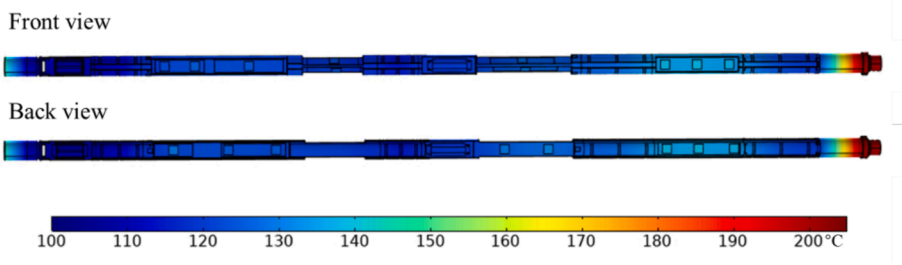

Fig. 9. The temperature contours of the TMS for SCT at the final moment (21 h).

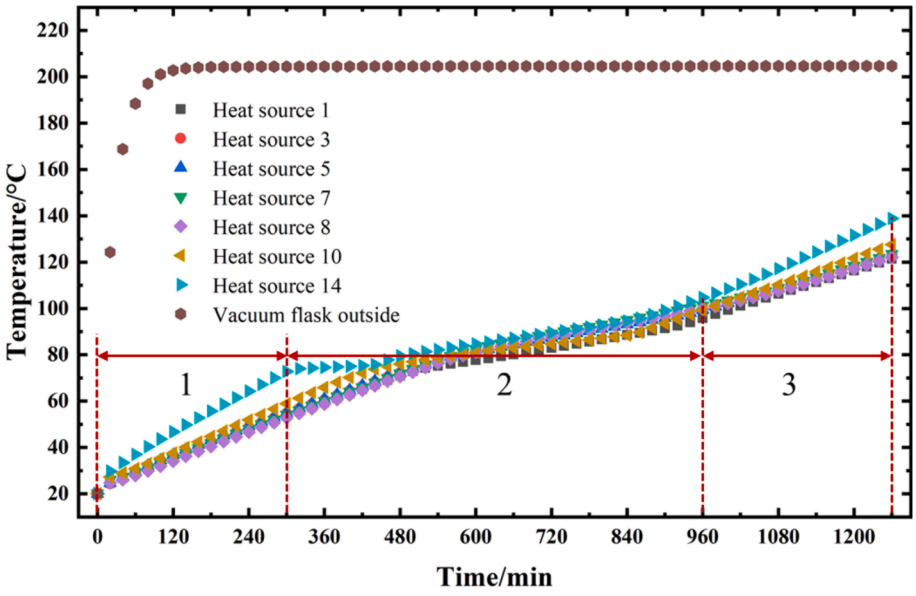

Fig. 10. The temperature curves of the vacuum flask and critical heat sources with time.

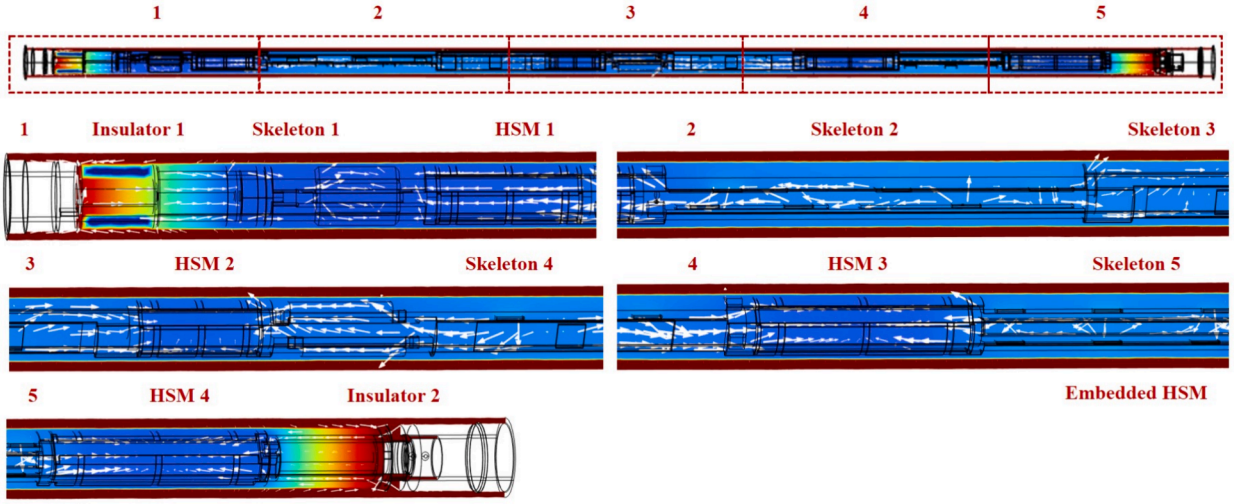

Fig. 11. The heat flow distribution of the proposed TMS at 600 min.

neighbouring HSMs. Notably, the highest temperature region within the skeleton and HSMs corresponds to skeleton 5, attributed to the electronics on it consuming the highest heating power of 20 W. In summary, the temperatures of the heat sources, skeletons, and HSMs exhibit remarkable uniformity, not exceeding 150 °C, which is attributed to repeated iterations of the optimized design.

Fig. 10 displays the temperature curves of the vacuum flask and critical heat sources with time. The temperature of the vacuum flask rises to 205 °C within 2 h and then stabilizes. Meanwhile, the internal heat sources maintain a consistently low temperature, due to the exceptional thermal insulation provided by the vacuum flask and insulators. The temperature profiles of all heat sources exhibit a rapid initial increase, followed by a gradual deceleration, and ultimately, another subsequence ascent. For instance, the temperature of the heat source 14 rises swiftly to 72 °C in the first 300 min, slowly increases to 104 °C between 300 and 960 min, and then experiences a rapid surge to 138.83 °C from 960 to 1260 min. The slow temperature rise is attributed to the phase change of the PCMs in the HSMs. After 21 h of operation, the final temperatures of heat source 1, 3, 5, 7, 8, 10, and 14 reach 121.37 °C, 123.09 °C, 123.22 °C, 123.50 °C, 122.17 °C, 127.59 °C, and 138.83 °C, respectively. The maximum temperature differences between the heat sources are within 12 °C. Importantly, all these temperatures fall within the acceptable range for downhole electronics, underscoring the efficacy of the TMS.

4.2. *Heat flow and phase transition analysis*

The heat flow and phase change processes are meticulously examined to underscore the advantages of the proposed TMS. Fig. 11 delineates the heat flow distribution of the proposed TMS at 600 min, elucidated in five distinct sections. The white arrows represent the direction of heat flow. The length of the arrows signifies the magnitude of the heat flow, and the coloration in the cloud diagram indicates temperature, with red denoting the highest temperature. In the first section encompassing insulator 1, skeleton 1, and HSM 1, minimal heat flows along the axial direction of the vacuum flask. This observation underscores the insulating capability of the vacuum flask, which effectively shields most of the heat from the environment. The heat circumvents the vacuum layer and permeates skeleton 1 from the end of the opening. The temperature of skeleton 1 without heat generation, is lower than that of

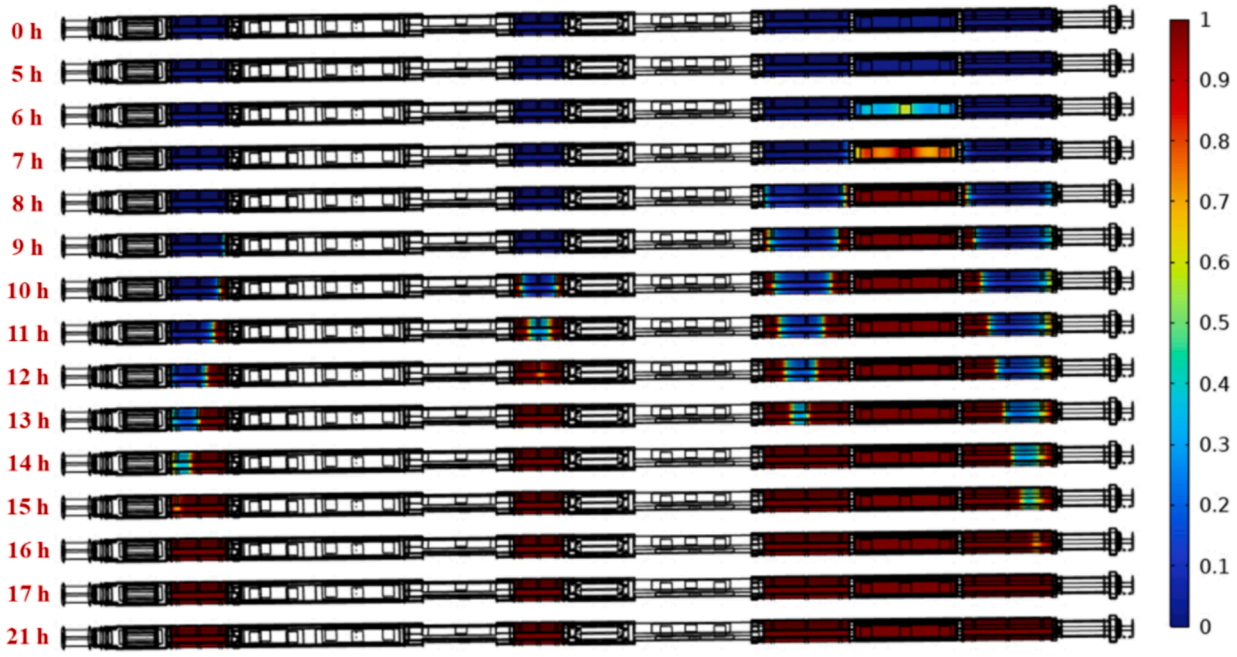

Fig. 12. The phase transition contours of the HSMs over time.

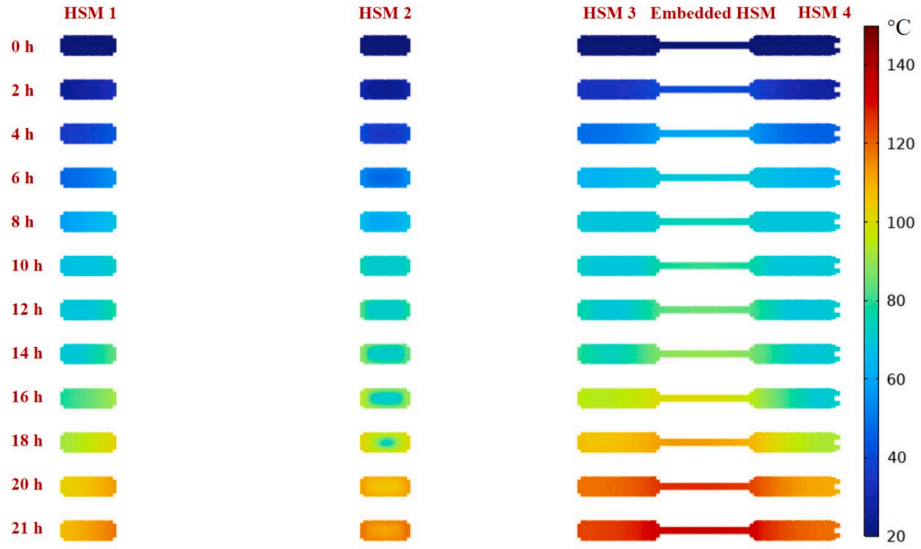

Fig. 13. The temperature contours of the HSMs over time.

HSM 1 due to insulator 1 impeding most of the heat flow. The second section involves HSM 1, skeleton 2, and skeleton 3. Due to the high heat generation on skeleton 2, a portion of the heat flow is directed to HSM 1, while the remainder is transferred to skeleton 3. Sections 3 and 4 depict the transfer of heat flow from skeleton 3 to HSM 2, while the heat flow from skeleton 4 is directed to both HSM 2 and HSM 3. The heat flow in the HSMs diminishes gradually until it dissipates. In section 4 and 5, the heat flow on skeleton 5 originates from the heat source and dissipates into HSM 3, embedded HSM and HSM 4. At the large opening of the vacuum flask, a portion of the environmental heat is transferred to HSM 4 and absorbed. Notably, the heat flow through the shell of insulator 2 far exceeds that of the core due to the core's low thermal conductivity. The rationale behind the proposed TMS is evident in the intricate distribution of heat flow.

Fig. 12 shows displays the phase transition contours of the HSMs over time, with 0 and 1 indicating the solid PCM and the liquid PCM, respectively. 0–1 indicate the solid–liquid mixing area of PCM, which reflects the phase change interface. The blue area represents the solid PCM, while the red area represents the liquid PCM, and the color between red and blue represents the solid–liquid PCM mixing area. The color change on the right side over time is from blue to red. The phase change region of the HSMs is from the sides to the center except for the embedded HSM. Due to the high heating power of the heat source on the skeleton 5, the embedded HSM located inside the skeleton 5 is the first to undergo a phase change from below the heat sources. Subsequently, the neighbouring HSM 3 and HSM 4 undergo a corresponding phase change, followed by the phase transition of HSM 1 and HSM 2. The direction of phase change in the HSMs is aligned with the direction of the heat flow. From the transition of the HSM 4, the heat transfer from the environment is less relative to the self-generated heat of the heat sources.

Fig. 13 shows temperature contours of the HSMs for the middle cross section over time. The temperatures of all HSMs are rising with time, and

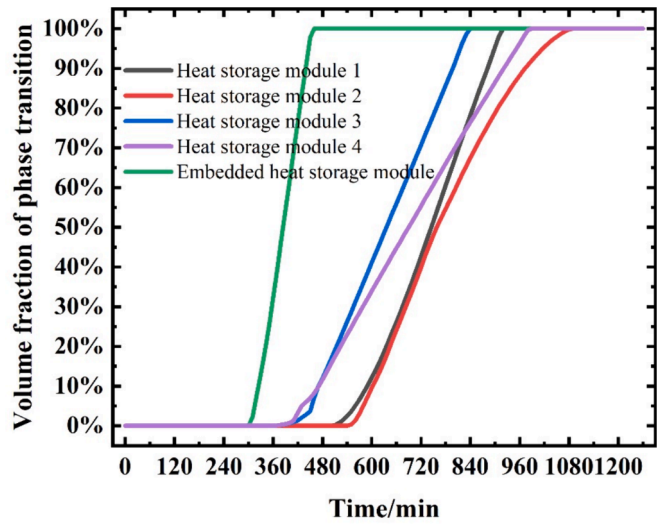

Fig. 14. The fraction of liquid PCMs curves as a percentage of volume over time.

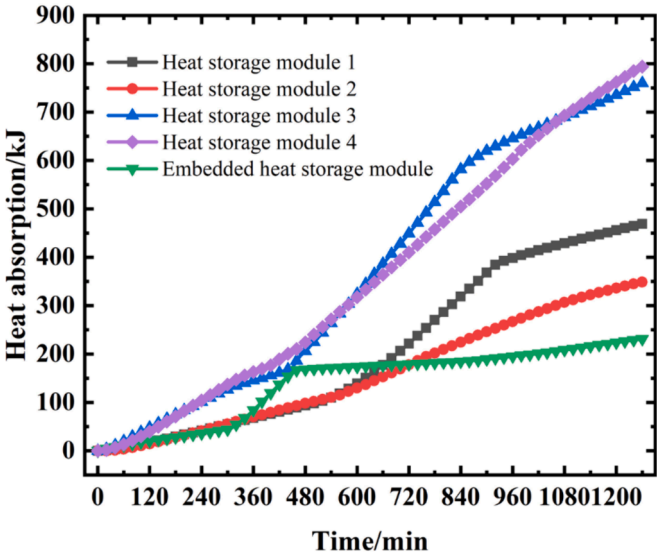

Fig. 15. The heat storage of the HSMs versus time.

the temperature difference between the HSMs is small. For each HSM, the temperatures show a tendency to be high at both ends and low in the middle, which is consistent with the phase transition trend of phase change materials. The temperature of the embedded HSM is uniformly increased due to the fact that located inside the skeleton 5. Fig. 14 displays the fraction of liquid PCMs curves as a percentage of volume over time. The phase change intervals for HSM 1, HSM 2, HSM 3, HSM 4, and the embedded HSM are 500–920 min, 530–1090 min, 340–840 min, 350–990 min, and 310–470 min, respectively. Notably, these phase change intervals align with the periods during which the temperature rise of the adjacent heat source experiences a deceleration.

4.3. Heat absorption and generation

The heat storage of the HSMs is further elucidated in Fig. 15. When the PCMs in the HSMs undergo no phase change or complete the phase transition, the HSMs store heat as sensible heat, leading to a rise in temperature. During the phase change process, the HSMs primarily absorb heat in the form of latent heat, resulting in minimal temperature change. Therefore, the heat absorption curve of the HSMs exhibits two

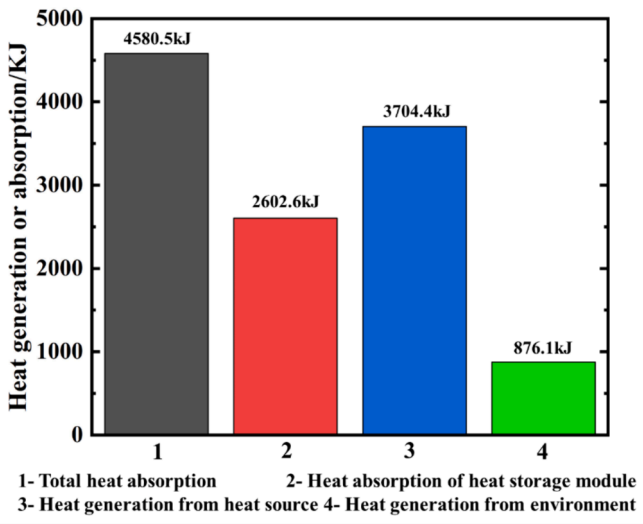

Fig. 16. The heat generation and absorption of the TMS.

inflection points, delineating the phase transition interval wherein the heat storage rate substantially increases. The heat storage in the HSMs and other parts can be calculated as:

$$Q_{storage} = \iiint \rho(H - H_0)dV \tag{8}$$

The heat absorption values for HSM 1, HSM 2, HSM 3, HSM 4, and the embedded HSM are 468.7 kJ, 349.0 kJ, 759.7 kJ, 793.9 kJ, and 231.2 kJ, respectively.

Fig. 16 shows the heat generation and absorption of the TMS. The total heat storage within the vacuum flask reaches 4580.5 kJ, with the HSMs contributing 2602.6 kJ. This implies that the heat storage of the HSMs constitutes 56.8 % of the total heat storage, underscoring the pivotal role played by the HSMs in the TMS. The total heat storage is equal to the sum of the heat generated by the heat sources and the heat leakage from the environment, which can be expressed as:

$$Q_{storage-total} = Q_{storage-HSMs} + Q_{storage-others} = Q_{heat} + Q_{environment} \tag{9}$$

The total heat generated by the heat sources amounts to 3704.4 kJ, so the heat originating from the environment is 876.1 kJ. This indicates that the vacuum flask and insulators effectively insulate the majority of the heat, and the heat within the vacuum flask is predominantly influenced by the heat generated by the heat source. The proposed TMS demonstrates outstanding performance in terms of heat production and storage, rendering it effective for prolonged durations.

4.4. Experimental verification

Fig. 17 presents the experimental temperature curves of the measuring points versus time. Since the measuring points is up to 16, they are divided into two figures for presentation. Fig. 17(a) shows that the ambient temperature rises to 205 °C within 60 min and remains stable, while the temperature of vacuum flask outside rises to 205 °C within 120 min. In contrast, the temperatures of the insulator 1, insulator 2 and the skeleton 1 are maintained at lower levels. This suggests that the vacuum flaks and insulators provide excellent thermal insulation. Furthermore, the temperature rise of the HSMs exhibits a distinct constant temperature plateau and a prolonged interval of constant temperature, indicating a significant heat storage effect. Fig. 17(b) shows the temperature rise of crucial heat sources. Notably, the temperature rise is more uniform for all heat sources, except for heat source 14. Each heat source's temperature rise exhibits a distinct region of slow temperature increase. After 21 h of operation, the final measured

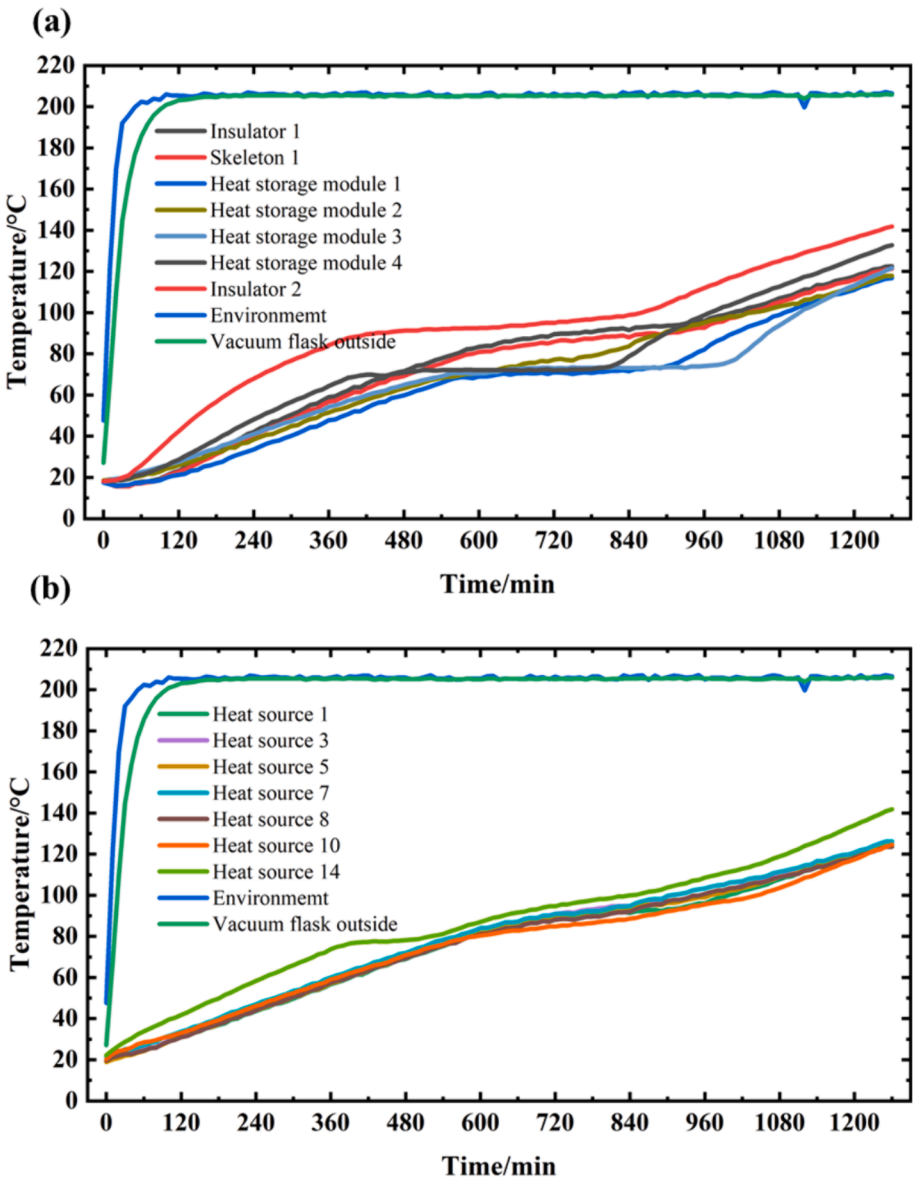

Fig. 17. The experimental temperature curves of the measuring points versus time: (a) The insulators, skeleton, and HSMs; (b) the crucial heat sources.

temperatures of heat source 1, heat source 3, heat source 5, heat source 7, heat source 8, heat source 10, and heat source 14 reach 124.3 °C, 125.1 °C, 124.4 °C, 126.3 °C, 123.7 °C, 124.6 °C, and 141.9 °C, respectively. Importantly, all temperatures fall within the normal operating range for electronics.

To verify the simulation, the simulated results is compared with experimental results, as depicted in Fig. 18. The dots indicate simulated results, and the lines indicate experimental results. The temperature rise curves obtained from experiments exhibit a similar trend to those obtained from simulations. At the final moment, the discrepancy between experiment and simulation does not exceed 5 °C, with a relative error of less than 5 %. This shows that the results of numerical simulations are convincing. Furthermore, an exploration into the reasons behind the deviation between the experiment and simulation is conducted. The errors primarily derived from the assumptions made in the simulation and the experimental conditions. Firstly, the neglect of thermal convection and thermal radiation inside the vacuum flask weakens the heat transfer between the flask and the skeleton, resulting in reduced simulated temperatures for the skeleton and heat source. Secondly, by disregarding contact thermal resistance, the thermal resistance between neighbouring components decreases, thus lowering the simulated temperature. Consequently, the enhanced heat transfer between heat sources leads to increased heat transfer between the heat source and the PCM, resulting in a lower simulated temperature for the PCM. Thirdly, although there were slight variations in initial temperatures among skeletons during the experiment, these minor temperature difference had a minimal impact on the results.

4.5. *Comparison with previous work*

To demonstrate the superiority of the proposed TMS, we compared our work with previous works [34–36]. The heating power, the total length, operating time and temperature difference of previous works was shown in Table 6. Fig. 19 shows the maximum temperature curves of the heat sources in this work and previous works. In previous work 1, Zhang et. al [36] optimized the TMS, and the maximum temperature of the heat sources reached 123 °C after 6 h with the temperature difference more than 30 °C. Lan et. al [35] proposed a distributed heat storage system for a multi-heat source logging tool, ensuring the maximum temperature of the heat sources stayed below 150 °C after 9 h operation in previous work 2 with the temperature difference more than 60 °C. Peng et al. [34] established a heat transfer channel between electronics

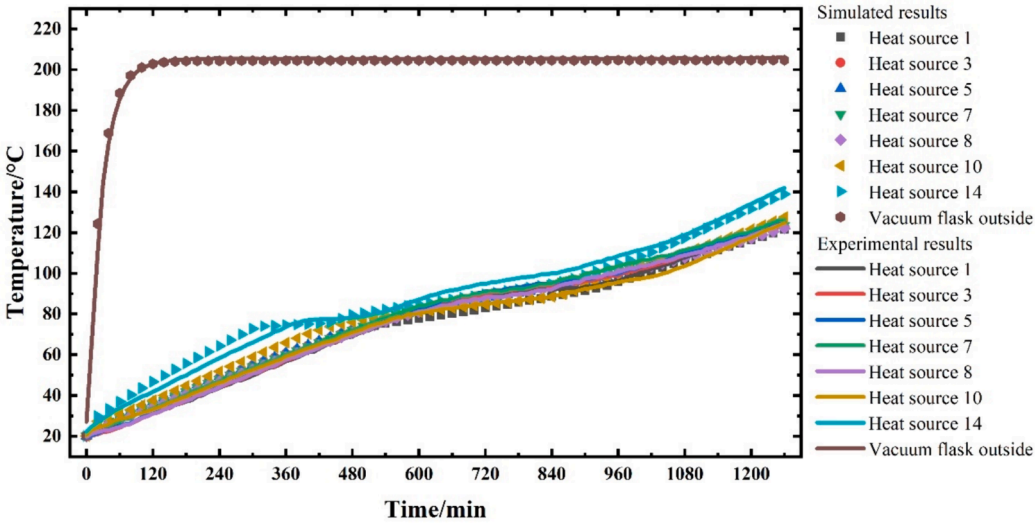

Fig. 18. The comparison of experimental and simulated results.

Table 6
The heating power and the total length of previous works.

	Heating power	Total length	Operating time	Temperature difference
Zhang's work	30 W	900 mm	6 h	More than 30 °C
Lan's work	90 W	4050 mm	9 h	More than 60 °C
Peng's work	25 W	1069 mm	9 h	51.3 °C
This work	49 W	4092.5 mm	21 h	18.2 °C

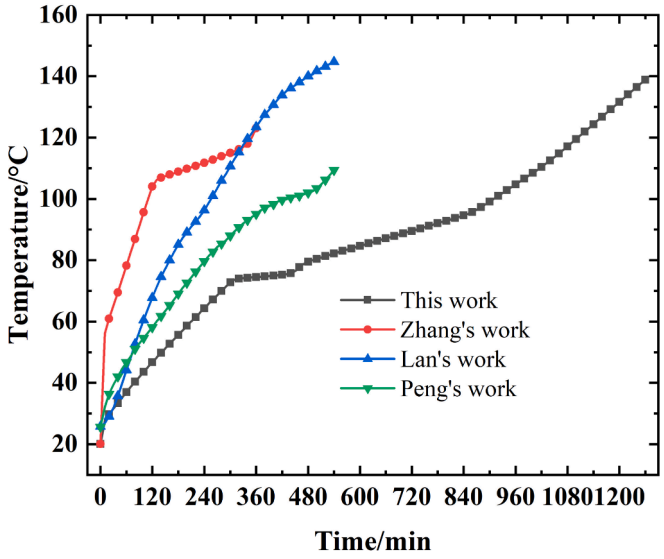

Fig. 19. The maximum temperature curves of the heat sources in this work and previous works [33–35].

and PCM, maintaining the heat sources below 120 °C for 9 h with the temperature difference 51.3 °C at an ambient temperature of 205 °C. In comparison, the maximum temperature of the heat source in this work does not exceed 140 °C in 21 h, and the temperature rise curve is slower compared to the previous work. In addition, the temperature uniformity significantly improves compared to the previous works, and the maximum temperature between the heat sources and HSMs was no more than 18.2 °C.

Table 7
Part of the statistical table for SCT.

	Location	Depth (m)	Temperature (°C)	specific gravity of slurry (sg)
1	South China Sea	5627	192	2.23
2	South China Sea	5023	172	1.39
3	South China Sea	4916	156	2.04
4	South China Sea	3983	145	1.36
5	East China Sea	4658	184	1.37
6	Bohai Sea	4792	161	1.62

The enhanced performance is credited to the iterative design process and the development of the HSMs. The heat source was distributed on the skeletons according the heating power, and the heat generated by the heat sources was quickly absorbed by the neighboring HSMs, reducing the heat transfer thermal resistance. In addition, the PCMs encapsulated inside the HSM were low melting point alloys with high thermal conductivity, which can quickly absorb the heat generated by the heat sources. Finally, the Nelder-Mead algorithm was used to thermally optimize the system for a certain length, which further promoted the system temperature uniformity. Temperature uniformity was promoted by the three means mentioned above and the heat storage was increased. Furthermore, the SCT has successfully performed more than 50 coring operations. Table 7 shows part of the statistical table for SCT. The challenges faced in real-world downhole applications was high-temperature vibration environments. The proposed TMS for the SCT has proven its durability and reliability through successful applications in numerous downhole operations.

5. Conclusions

We proposed a durable reliable thermal management system (TMS) with superior temperature uniform for the sidewall coring tool (SCT) to protect the internal electronics operating in extreme thermal environments. The system adopted a rational design after iterative optimization to achieve the temperature uniformity. Additionally, we have developed heat storage modules (HSMs) with high reliability and a substantial capacity for storing heat, thereby extending the operational duration of the electronic heat source. The high-temperature vibration reliability of

HMSs has been verified through extensive experimental tests. Simulated results demonstrate that after operating at an ambient temperature of 205 °C for 21 h, the maximum temperature of all heat sources reached 138.83 °C, with a maximum temperature difference between any two sources not exceeding 12 °C. The total heat amounts to 4580.5 kJ, with only 876.1 kJ originating from the environment, and the heat storage of the HSMs constitutes 56.8 % of the total heat storage. The experimental results validated the simulated results with the relative error within 5 %. The maximum temperature of heat sources in the experiment was 141.9 °C after 21 h operation, differing from the simulation by only 3.07 °C. In addition, compared to the previous works, the working time of the proposed system has improved significantly. Furthermore, the proposed TMS for the SCT has proven its durability and reliability through successful applications in numerous downhole operations. Therefore, the proposed TMS is promising for utilization in other logging tools operating under similar conditions as SCT with the ambient temperature not exceeding 205 °C and vibration acceleration not greater than 10 g. Due to the excellent thermal insulation properties of the proposed TMS, it is difficult to cool down after completing the operation. Therefore, improvements based on the proposed TMS are needed in future work to promote rapid cooling down of the system.

CRediT authorship contribution statement

Jiale Peng: Writing – original draft, Visualization, Validation, Software, Methodology, Investigation, Formal analysis, Data curation, Conceptualization. **Zhibin Tian:** Investigation, Data curation. **Chao Deng:** Investigation, Data curation. **Fulong Wei:** Methodology, Data curation. **Bofeng Shang:** Writing – review & editing, Supervision, Funding acquisition. **Xiaobing Luo:** Writing – review & editing, Supervision, Funding acquisition.

Declaration of competing interest

The authors declare that they have no known competing financial interests or personal relationships that could have appeared to influence the work reported in this paper.

Data availability

Data will be made available on request.

Acknowledgement

This research was supported by the Open Fund Science and Technology on Thermal Energy and Power Laboratory (No. TPL2022B02) and the Natural Science Foundation of Henan Province (Grant No. 222300420310).

References

[1] H. Wang, Y. Ge, L. Shi, Technologies in deep and ultra-deep well drilling: Present status, challenges and future trend in the 13th Five-Year Plan period (2016–2020), Nat. Gas Industry B. 4 (2017) 319–326.
[2] X. He, G. Chen, J. Wu, Y. Liu, S. Wu, J. Zhang, et al., Deep shale gas exploration and development in the southern Sichuan Basin: New progress and challenges, Nat. Gas Ind. B 10 (2023) 32–43.
[3] M. Macenić, T. Kurevija, I. Medved, Novel geothermal gradient map of the Croatian part of the Pannonian Basin System based on data interpretation from 154 deep exploration wells, Renew. Sustain. Energy Rev. 132 (2020) 110069.
[4] G. Zhai, J. Hu, W. Zhao, C. Zcou, History, achievements and significance of scientific exploration wells: For the 30th anniversary of the Scientific Exploration Well Program, Petrol Explor Dev. 43 (2016) 167–181.
[5] H. Yang, J. Li, H. Zhang, J. Jiang, B. Guo, R. Gao, et al., Thermal behavior prediction and adaptation analysis of a reelwell drilling method for closed-loop geothermal system, Appl. Energy 320 (2022) 119339.
[6] M. Yang, D. Luo, Y. Chen, G. Li, D. Tang, Y. Meng, Establishing a practical method to accurately determine and manage wellbore thermal behavior in high-temperature drilling, Appl. Energy 238 (2019) 1471–1483.
[7] C. Dai, J. Li, Y. Shi, L. Zeng, H. Lei, An experiment on heat extraction from a deep geothermal well using a downhole coaxial open loop design, Appl. Energy 252 (2019) 113447.
[8] J. Charlie, Tutorial: A century of sidewall coring evolution and challenges, from shallow land to deep water, Petrophysics. 62 (2021) 230–243.
[9] G. Webster, G. Dawsongrove, The alteration of rock properties by percussion sidewall coring, J Pet Technol. 11 (1959) 59–62.
[10] A. Neal, M. Ashton, M. Bowman, C.Y. Hern, B. Levell, The role of core in twenty-first century reservoir characterization: an introduction, Geol. Soc. Lond. Spec. Publ. 527 (2022) 1–15.
[11] P. Mahzari, T.M. Mitchell, A.P. Jones, D. Westacott, A. Striolo, Direct gas-in-place measurements prove much higher production potential than expected for shale formations, SCI REP-UK 11 (2021) 10775.
[12] C. Jackson, Rotary sidewall coring advancements for deep water, including a coring background overview. In the SPWLA 61st Annual Logging Symposium, Virtual Online Webinar, June 2020, 2020.
[13] V. Khanna, Extreme-Temperature and Harsh-Environment Electronics: Physics, Technology And Applications, IOP Publishing, 2023.
[14] L. Wang, C. Yang, X. Wang, J. Shen, W. Sun, J. Wang, et al., Advances in polymers and composite dielectrics for thermal transport and high-temperature applications, Compos. A Appl. Sci. Manuf. 164 (2023) 107320.
[15] J. Peng, W. Lan, F. Wei, C. Deng, X. Luo, Thermal management for high-power downhole electronics using liquid cooling and PCM under high temperature environment, in: 2022 IEEE 24th Electronics Packaging Technology Conference (EPTC), 2022, pp. 935–940.
[16] Y. Lv, W. Chu, Q. Wang, Thermal management systems for electronics using in deep downhole environment: A review, Int. Commun. Heat Mass Transfer 139 (2022) 106450.
[17] M. Wei, W. Cai, M. Xu, S. Deng, Active cooling system for downhole electronics in high-temperature environments, J. Therm. Sci. Eng. Appl. 14 (2022) 081009.
[18] Q. Tao, M. Wei, H. Chen, A. Deng, Y. He, Thermal management system of vapor compression for downhole instrument, J. Therm. Sci. Eng. Appl. 15 (2023) 091005.
[19] S. Soprani, J. Haertel, B. Lazarov, O. Sigmund, K. Engelbrecht, A design approach for integrating thermoelectric devices using topology optimization, Appl. Energy 176 (2016) 49–64.
[20] R. Weerasinghe, T. Hughes, Analysis of thermal performance of geophonic downhole measuring tools; a numerical and experimental investigation, Appl. Therm. Eng. 137 (2018) 504–512.
[21] S. Tang, W. Gao, K. Liu, Design and numerical study of active cooling system of measurement while drilling for high temperature based on supersonic, Case Studies in Thermal Engineering. 50 (2023) 103460.
[22] S. Ma, S. Zhang, J. Wu, et al., Experimental study on active thermal protection for electronic devices used in deep− downhole− Environment exploration, Energies 16 (3) (2023) 1231.
[23] J. Peng, C. Deng, F. Wei, S. Ding, R. Hu, X. Luo, A hybrid thermal management system combining liquid cooling and phase change material for downhole electronics, J. Energy Storage. 72 (2023) 108610.
[24] S. Tang, Z. Liang, Y. Zhu, Numerical Investigation on Heat Transfer Characteristics in Electronic Cavity of Downhole Measurement-While-Drilling System, J. Therm. Sci. Eng. Appl. 13 (2021) 011022.
[25] W. Gao, K. Liu, X. Dou, L. Zhang, S. Tang, Numerical investigation on heat transfer rate from the outside environment into the electronic compartment of the measurement-while-drilling tools, Heat Transfer. 50 (2021) 5835–5852.
[26] J. Peng, Y. Wang, S. Ding, C. Deng, F. Wei, X. Luo, Rapid detection of the vacuum failure of logging tools based on the variation in equivalent thermal conductivity, Int. J. Therm. Sci. 188 (2023) 108245.
[27] F. Wei, C. Deng, J. Peng, et al., Thermal optimization of a logging tool used in high temperature downhole environment, in: 2022 IEEE International Power Electronics and Application Conference and Exposition (PEAC), IEEE, 2022, pp. 72–77.
[28] S. Rafie, Thermal management of downhole oil & gas logging sensors for hthp applications using nanoporous materials, in: Proceedings of 2nd Energy Nanotechnology International Conference, 2007, pp. S910–S931.
[29] S. Soprani, A.J. Nørgaard, C. Nesgaard, K. Engelbrecht, Design and testing of a heat transfer sensor for well exploration tools, Appl. Therm. Eng. 141 (2018) 887–897.
[30] C. Deng, F. Wei, W. Lan, et al., Experimental and numerical investigation of low melting point alloy for downhole electronics at high temperature, in: 2022 IEEE International Power Electronics and Application Conference and Exposition (PEAC), IEEE, 2022, pp. 49–54.
[31] J. Peng, W. Lan, F. Wei, C. Deng, B. Xie, X. Luo, A numerical model coupling multiple heat transfer modes to develop a passive thermal management system for logging tool, Appl. Therm. Eng. 223 (2023) 120011.
[32] Y. Ma, B. Shang, R. Hu, X. Luo, Thermal management of downhole electronics cooling in oil & gas well logging at high temperature, in: 2016 17th international conference on electronic packaging technology (ICEPT), 2016, pp. 623–627.
[33] B. Shang, Y. Ma, R. Hu, C. Yuan, J. Hu, X. Luo, Passive thermal management system for downhole electronics in harsh thermal environments, Appl Them Eng. 118 (2017) 593–599.
[34] J. Peng, W. Lan, Y. Wang, Y. Ma, X. Luo, Thermal management of the high-power electronics in high temperature downhole environment, in: IEEE 22nd Electronics Packaging Technology Conference (EPTC), 2020, pp. 369–375.
[35] W. Lan, J. Zhang, J. Peng, Y. Ma, S. Zhou, X. Luo, Distributed thermal management system for downhole electronics at high temperature, Appl. Therm. Eng. 180 (2020) 115853.
[36] J. Zhang, W. Lan, C. Deng, F. Wei, X. Luo, Thermal optimization of high-temperature downhole electronic devices, IEEE Trans. Compon. Packag. Manuf. Technol. 11 (2021) 1816–1823.

[37] J. He, Q. Wang, J. Wu, Y. Zhang, W. Chu, Hybrid thermal management strategy with PCM and insulation materials for pulsed-power source controller in extreme oil-well thermal environment, Appl. Therm. Eng. 214 (2022) 118864.
[38] S. Costa, M. Kenisarin, A review of metallic materials for latent heat thermal energy storage: Thermophysical properties, applications, and challenges, Renew. Sust. Energ. Rev. 154 (2022) 111812.
[39] K. Chen, X. Wei, J. Ding, W. Wang, J. Lu, Bi-Sn-In phase change material with low melting point and high cyclic stability for thermal energy storage and management, Chem. Eng. J. 435 (2022) 135055.
[40] B. Shang, R. Wu, J. Hu, R. Hu, X. Luo, Non-monotonously tuning thermal conductivity of graphite-nanosheets/ paraffin composite by ultrasonic exfoliation, Int. J. Therm. Sci. 131 (2018) 20–26.
[41] B. Shang, J. Hu, R. Hu, J. Cheng, X. Luo, Modularized thermal storage unit of metal foam/paraffin composite, Int J Heat Mass Tran. 125 (2018) 596–603.
[42] J. Peng, W. Lan, C. Deng, F. Wei, S. Ding, R. Hu, B. Shang, X. Luo, An improved numerical model based on the equivalent thermal conductivity method for downhole thermal management systems, Int Commun Heat Mass. 152 (2024) 107317.
[43] Y. Hu, R. Guo, P. Heiselberg, H. Johra, Modeling PCM phase change temperature and hysteresis in ventilation cooling and heating applications, Energies 13 (23) (2020) 6455.